

# Electrochemical Properties of APCVD $\alpha$ -Fe<sub>2</sub>O<sub>3</sub> Nanoparticles at 300 °C

Dimitra Vernardou,<sup>\*,[a]</sup> Maria Apostolopoulou,<sup>[a]</sup> Nikolaos Katsarakis,<sup>[a, b]</sup> Emmanouil Koudoumas,<sup>[a, b]</sup> Charalampos Drosos,<sup>[c]</sup> and Ivan P. Parkin<sup>\*,[c]</sup>

The growth of hematite (Fe<sup>III</sup> oxide) by atmospheric pressure chemical vapor deposition was possible at 300 °C by controlling the nitrogen flow rate through the iron precursor bubbler. An increase of crystallinity along with the presence of compact interconnected nanoparticles was observed upon increasing the nitrogen flow rate. The amount of incorporated charge was the highest for the 0.6 L min<sup>-1</sup> coating presenting reversibility

after a period of 1400 s as obtained from chronoamperometry measurements. Additionally, the charge transfer of lithium-ions across the Fe<sup>III</sup> oxide / electrolyte interface was easier enhancing its performance presenting capacitance retention of 94% after 500 scans. The importance of nitrogen flow rate towards the deposition of an anode with good stability and effective electrochemical behavior is highlighted.

## 1. Introduction

Rechargeable Li-ion batteries are considered as the leading candidates for power sources of electric vehicles because of their high energy density, small size and light weight.<sup>[1]</sup> However, the performance of current electrode materials cannot meet the challenge of increasing demand for high capacity and/or high power. To achieve high performance economic Li-ion batteries, the growth of anode materials with high efficiency, long cycle life and no-toxicity is essential.<sup>[2-6]</sup>

Hematite ( $\alpha$ -Fe<sub>2</sub>O<sub>3</sub>) has been investigated as anode material because of its higher theoretical specific capacity (1007 mAh g<sup>-1</sup>)<sup>[7]</sup> compared with the conventional graphite (372 mAh g<sup>-1</sup>)<sup>[8]</sup> nontoxicity, low cost and natural abundance<sup>[9,10]</sup>. During cycling of Li<sup>+</sup> intercalation/deintercalation, hematite breaks into small metal clusters because it reacts with Li to form Li<sub>2</sub>O,<sup>[11]</sup> leading to a large volume expansion and a destruction of the structure upon electrochemical cycling resulting in loss of capacity with cycling and a low electrical conductivity.<sup>[12]</sup> The overall electrochemical reaction involves a displacement reaction in Fe<sup>III</sup> oxide as follows in equation (1):<sup>[13]</sup>

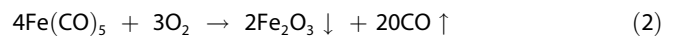


The reversible and rate capacity of  $\alpha$ -Fe<sub>2</sub>O<sub>3</sub> can be improved through the development of nanostructures, which can be attributed to shortened Li<sup>+</sup> intercalation/deintercalation pathways.<sup>[14,15]</sup> Extensive efforts have been focused on controlling the nanostructures of  $\alpha$ -Fe<sub>2</sub>O<sub>3</sub> through physical (molecular beam epitaxy,<sup>[16]</sup> reactive sputtering,<sup>[17]</sup> pulsed laser deposition<sup>[18]</sup>) and chemical methods (sol-gel,<sup>[19]</sup> electrochemical synthesis,<sup>[20]</sup> ultrasonic spray pyrolysis<sup>[21]</sup>, one-pot hydrothermal synthesis<sup>[22]</sup> and chemical vapor deposition<sup>[23,24]</sup>). Among the various methods utilized, chemical vapor deposition at atmospheric pressure (APCVD) can provide uniform coatings over large areas at low temperatures and can be compatible with high-volume glass manufacturing lines. Hence, several studies have been reported using ferrocene,<sup>[25-27]</sup> [Fe<sub>6</sub>(PhCOO)<sub>10</sub>(acac)<sub>2</sub>(O)<sub>2</sub>(OH)<sub>2</sub>]<sub>3</sub>C<sub>7</sub>H<sub>8</sub>,<sup>[28]</sup> iron acetylacetonate<sup>[29]</sup> and tris(*t*-butyl-3-oxo-butanoato)Fe<sup>III</sup><sup>[30]</sup>.

In this paper, the APCVD of iron pentacarbonyl (Fe(CO)<sub>5</sub>)<sup>[31-34]</sup> to produce  $\alpha$ -Fe<sub>2</sub>O<sub>3</sub> coatings on fluorine doped SnO<sub>2</sub> (FTO)-precoated glass substrates at 300 °C is presented. The choice of this precursor is desirable for handling reasons (vapor pressure 35 mmHg at 25 °C) since its decomposition over time and transport of unknown species are avoided. Moreover, this work provides an understanding of the coatings characteristics-property relationship for the use of Fe<sub>2</sub>O<sub>3</sub> as anodes.

## 2. Results and Discussion

A volatile precursor source such as Fe(CO)<sub>5</sub> was carried with N<sub>2</sub> along with O<sub>2</sub> gas over the heated substrate in the reaction chamber for Fe<sub>2</sub>O<sub>3</sub> deposition to take place on the surface of the substrate as shown in equation (2) below



The properties of the deposit were changed by varying the

[a] Dr. D. Vernardou, M. Apostolopoulou, Prof. N. Katsarakis, Prof. E. Koudoumas  
Center of Materials Technology and Photonics, School of Engineering, Technological Educational Institute of Crete, 710 04 Heraklion, Crete, Greece  
E-mail: dvernardou@staff.teicrete.gr

[b] Prof. N. Katsarakis, Prof. E. Koudoumas  
Electrical Engineering Department, Technological Educational Institute of Crete, 710 04 Heraklion, Crete, Greece

[c] C. Drosos, Prof. I. P. Parkin  
Department of Chemistry, University College London, 20 Gordon Street, London WC1H 0AJ, United Kingdom  
E-mail: i.p.parkin@ucl.ac.uk

composition of gas ( $N_2/O_2$ ) for constant  $O_2$  flow rate. A general observation was that there was no efficient deposition for  $N_2$  flow rates through the  $Fe(CO)_5$  bubbler  $< 0.2 L min^{-1}$ . This is in agreement with the growth rates derived, i.e. being  $90 nm min^{-1}$  ( $180 nm$ ),  $40 (80 nm)$  and  $25 nm min^{-1}$  ( $50 nm$ ) for  $0.6, 0.4$  and  $0.2 L min^{-1}$ , respectively. The growth rate was estimated from the deposition time and the coating's thickness as determined from profilometer. This behaviour may be due to the increased collision rate of the species in the gas-phase with those adsorbed on the substrate at the highest incoming flow resulting in higher  $Fe^{III}$  oxide species concentration. Additionally, in order to avoid blockages in bubbler lines or stainless steel lines due to rapid growth of  $Fe(CO)_5$  against temperature, it was decided to keep the maximum flow rate at  $0.6 L min^{-1}$  simultaneously with lower temperature at  $300 ^\circ C$ . Hence, this amount of  $N_2$  flow rate through the iron precursor bubbler appears to be necessary to ensure good step coverage throughout the substrate's surface. Only the as-grown coating for  $0.6 L min^{-1}$  passed the Scotch tape test (removal of an X shaped piece of sticking tape<sup>[35]</sup>) and was resistant to water. Furthermore, it had similar structural, morphological and electrochemical characteristics after storage for five months in air indicating long term stability under environmental conditions.

## 2.1. Structure

Figure 1 indicates the XRD of the as-grown coatings for  $N_2$  flow rate through the iron precursor bubbler of  $0.2, 0.4$  and  $0.6 L min^{-1}$ . Only the  $0.6 L min^{-1}$  presents one peak at  $33.23 ^\circ$  with Miller index (104).<sup>[36]</sup> Additionally, peaks at  $26.5, 33.7$  and  $37.1 ^\circ$  with Miller indices (110), (101) and (200), respectively corresponding to the FTO glass substrate are mainly observed for the lower  $N_2$  flow rates.<sup>[37]</sup> This behavior is expected because of the enhanced surface mobility with the  $N_2$  flow rate increases.

All Raman peaks in Figure 2 can also be indexed to  $\alpha-Fe_2O_3$ :  $A_{1g}$  ( $225 cm^{-1}$ ),  $E_g$  ( $292, 409$  and  $610 cm^{-1}$ ) and second harmonic vibration ( $1320 cm^{-1}$ ).<sup>[38-40]</sup> A significant increase in the signal-to-noise ratio was observed as the  $N_2$  flow rate increased from  $0.2$  to  $0.6 L min^{-1}$ , the Raman peaks becoming more intense and narrow. This reveals a trend towards ordering i.e. towards proliferation of crystalline domains that are however still small enough for  $0.2$  and  $0.4 L min^{-1}$  to lie below the detection limit of XRD.<sup>[41]</sup> Hence, these samples are mainly amorphous retaining however a short-range crystalline ordering that degrades with a reduction in  $N_2$  flow rate. The fact that their XRD and Raman patterns do not have discrepancies among each other as shown in Figures 1 and 2 may be related with their similarity in thickness values.

Figure 3 (a) presents the Fe 2p XPS spectrum of the as-grown coating for  $0.6 L min^{-1} N_2$  flow rate through the iron precursor bubbler. It can be Gaussian fitted into two peaks at  $711.29$  and  $724.63 eV$  corresponding to the binding energies of Fe  $2p_{3/2}$  and Fe  $2p_{1/2}$ , respectively, with an energy separation between the spin-orbit doublet of  $13.13 eV$  indicating the existence of the oxidation state of  $Fe^{3+}$ .<sup>[42,43]</sup> Two shake-up satellites are also observed at  $718.63$  and  $532.90 eV$ , which are the finger points of the electronic structure of  $Fe^{3+}$ , confirming the

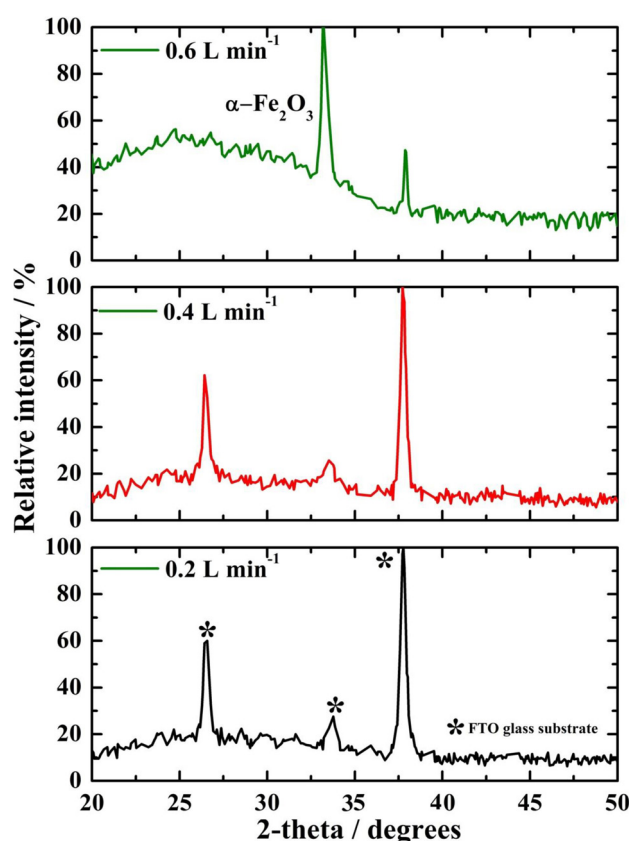


**Figure 1.** XRD of APCVD  $Fe^{III}$  oxides coatings at  $300 ^\circ C$  for  $0.2, 0.4$  and  $0.6 L min^{-1} N_2$  flow rate through the  $Fe(CO)_5$  bubbler.

formation of  $\alpha-Fe_2O_3$ .<sup>[16]</sup> Figure 3 (b) indicates the O 1s spectrum, which is asymmetrical with an obvious shoulder and can be deconvoluted into two peaks at  $530.10$  and  $532.68 eV$ . The first one is in good agreement with crystal lattice oxygen ( $O^{2-}$ ), while the highest binding energy is attributed to chemisorbed  $O^{2-}$  species on the surface.<sup>[44-46]</sup>

Additionally, EDS analysis confirmed that the as-grown coating for  $0.6 L min^{-1} N_2$  flow rate is pure  $Fe^{III}$  oxide as no other elements were detected (see Figure 4). Although, EDS is not accurate in measuring the concentration of light elements such as oxygen, the elemental ratio of iron to oxygen is estimated to be  $0.67$ , which corresponds to the composition of  $Fe_2O_3$ .

## 2.2. Morphology

Field-emission scanning electron microscopy images of the as-grown coatings for  $0.2$  and  $0.6 L min^{-1} N_2$  flow rate through the iron precursor bubbler are shown in Figure 5. They display uniform covering of porous microstructure composed of interconnected nanoparticles, which become compact for the highest flow rate. Hence, one may say that there is a dependence of growth rate (see above) on  $N_2$  flow rate. These porous microstructures can foster ion transport and diffusion through electrodes.<sup>[47]</sup>

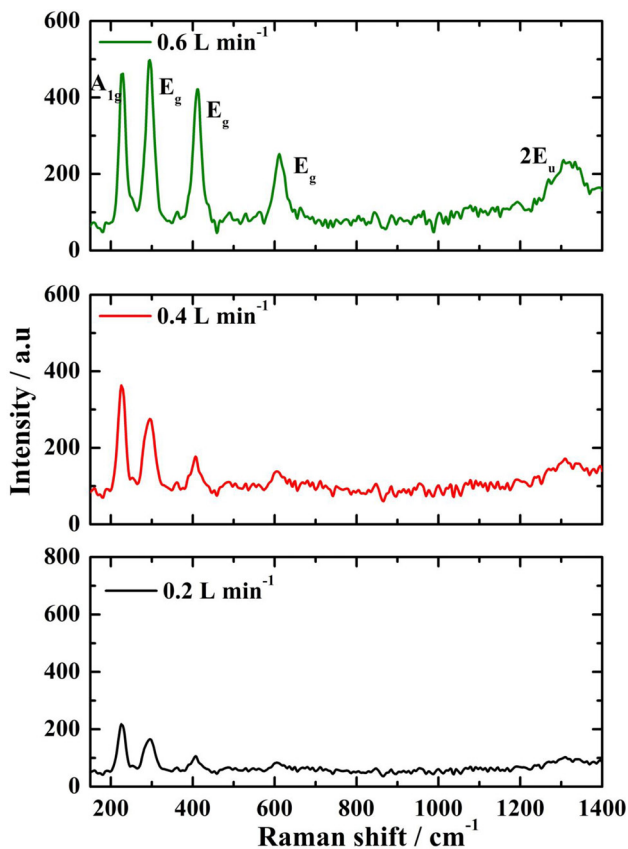


**Figure 2.** Raman spectra of APCVD Fe<sup>III</sup> oxides coatings at 300 °C for 0.2, 0.4 and 0.6 L min<sup>-1</sup> N<sub>2</sub> flow rate through the Fe(CO)<sub>5</sub> bubbler.

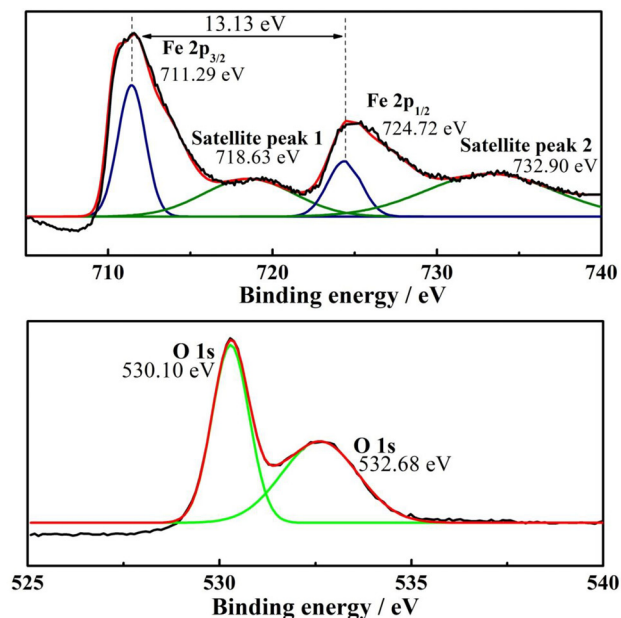


**Figure 3.** XPS in the Fe 2p and O 1s regions for the APCVD  $\alpha$ -Fe<sub>2</sub>O<sub>3</sub> for 0.6 L min<sup>-1</sup> N<sub>2</sub> flow rate through the Fe(CO)<sub>5</sub> bubbler.

### 2.3. Electrochemical Evaluation

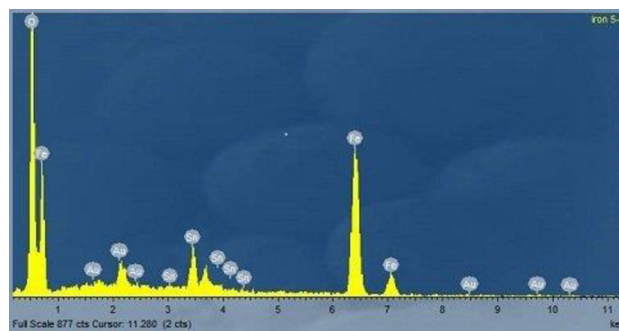


**Figure 4.** EDS of as grown  $\alpha$ -Fe<sub>2</sub>O<sub>3</sub> at 300 °C for 0.6 L min<sup>-1</sup> N<sub>2</sub> flow rate through the Fe(CO)<sub>5</sub> bubbler.

In order to investigate the effect of N<sub>2</sub> flow rate through the iron precursor bubbler on the electrochemical performance of the coatings, current-potential curves were obtained at a scan rate of 10 mV s<sup>-1</sup> sweeping the potential from -1 V to -0.2 V as shown in Figure 6. The curve obtained for 0.6 L min<sup>-1</sup> presents one cathodic peak at -0.6128 V and one anodic peak at -0.821 V, which are attributed to Li<sup>+</sup> intercalation and deintercalation accompanying gain and loss of an e<sup>-</sup>, respectively.<sup>[12,13,48]</sup> Furthermore, the current of this sample is the highest of all indicating an enhanced electrochemical activity. On the other hand, the shape of the curve for 0.2 L min<sup>-1</sup> is different, while the one for 0.4 L min<sup>-1</sup> presents less distinctive cathodic and anodic peaks at different positions. This discrepancy may be related with the existence of amorphous  $\alpha$ -Fe<sub>2</sub>O<sub>3</sub> compared with the 0.6 L min<sup>-1</sup> coating. Long-term degradation after the 50<sup>th</sup> scan for 0.2 and 0.4 L min<sup>-1</sup>, respectively was observed as evident from the decrease of current density by two degrees of magnitude (not shown here for brevity), while excellent stability is presented for the 0.6 L min<sup>-1</sup> as one can see from the similarity of the first and the 500<sup>th</sup> scan in Figure 6 inset.

One may then suggest that the highest amount of incorporated charge for the as-grown coating using 0.6 L min<sup>-1</sup> N<sub>2</sub> flow rate may be a combination of both structure (enhanced crystalline quality) and morphology (porous microstructure), which increases the active material exposed to the electrolyte.

To estimate the amount of lithium interchanged between the  $\alpha$ -Fe<sub>2</sub>O<sub>3</sub> and the electrolyte, chronoamperometric (CA) measurements were performed switching the potential between -1 V and -0.2 V at an interval of 200 s (per cycle) for a total period of 1400 s as shown in Figure 7 for the 0.6 L min<sup>-1</sup> coating.<sup>[49,50]</sup> It was found that the intercalated and deintercalated charges are similar to each other within 10% per cycle indicating the reversibility of the processes with the highest estimated charge being  $\approx 75$  C cm<sup>-2</sup>. On the other hand, the calculated charge intercalated was higher than the deintercalated for the lowest N<sub>2</sub> flow rates because Li<sup>+</sup> still remain in the oxide as also observed in other materials.

The chronopotentiometric (CP) curves of the as-grown coatings for 0.2, 0.4 and 0.6 L min<sup>-1</sup> N<sub>2</sub> flow rate through the iron precursor bubbler under a constant specific current of 1 A

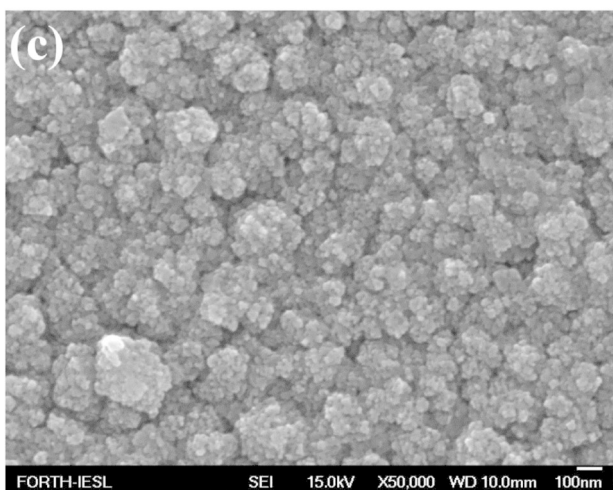
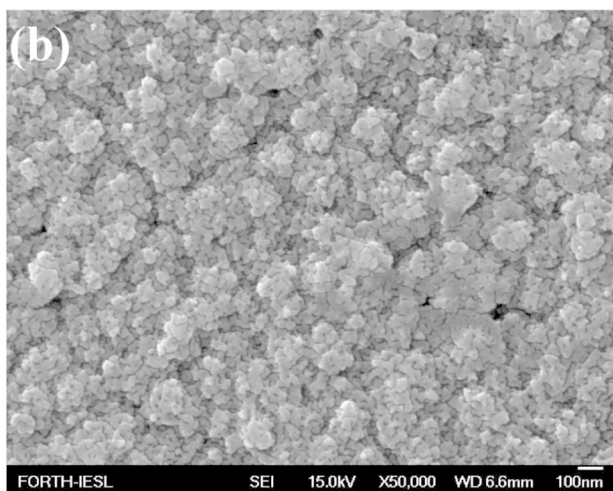
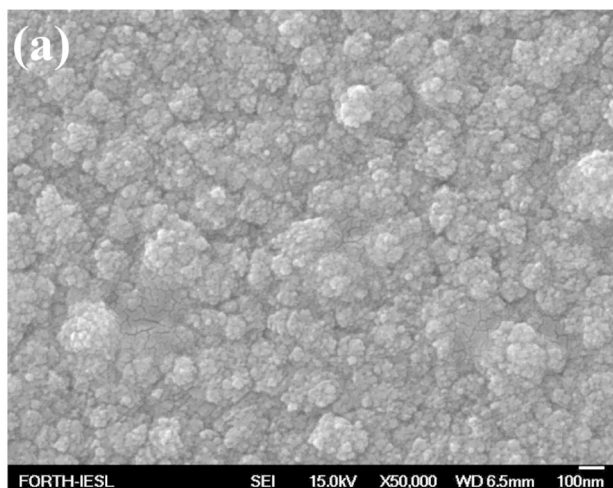


**Figure 5.** FE-SEM images of APCVD Fe<sup>III</sup> oxides coatings at 300 °C for 0.2 (a), 0.4 (b) and 0.6 L min<sup>-1</sup> (c) N<sub>2</sub> flow rate through the Fe(CO)<sub>5</sub> bubbler.

g<sup>-1</sup> and potential ranging from -0.2 to -1 V vs. Ag/AgCl are indicated in Figure 8. It is shown that the deintercalated (discharging) process is affected by the N<sub>2</sub> flow rate indicating one obvious plateau at -0.55 V and -0.45 V for 0.4 L min<sup>-1</sup> and 0.6 L min<sup>-1</sup>, respectively. On the other hand, the 0.2 L min<sup>-1</sup>

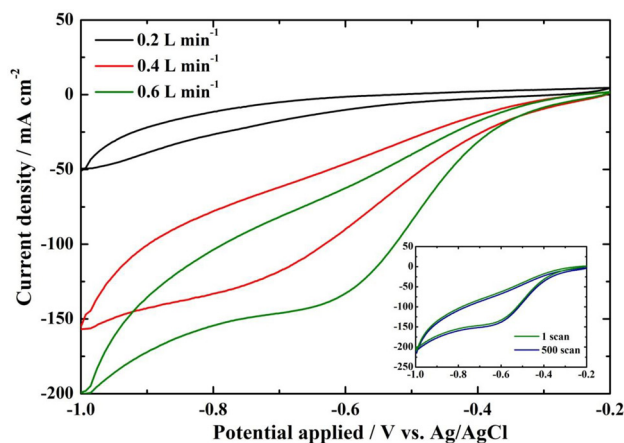


**Figure 6.** Cyclic voltammograms of the first scan for the APCVD Fe<sup>III</sup> oxides coatings at 300 °C for 0.2, 0.4 and 0.6 L min<sup>-1</sup> N<sub>2</sub> flow rate through the Fe(CO)<sub>5</sub> bubbler using a scan rate of 10 mV s<sup>-1</sup> and a working electrode geometrical area of 1 cm<sup>2</sup>. Cyclic voltammograms of the first and the 500<sup>th</sup> scan for the 0.6 L min<sup>-1</sup> as inset.

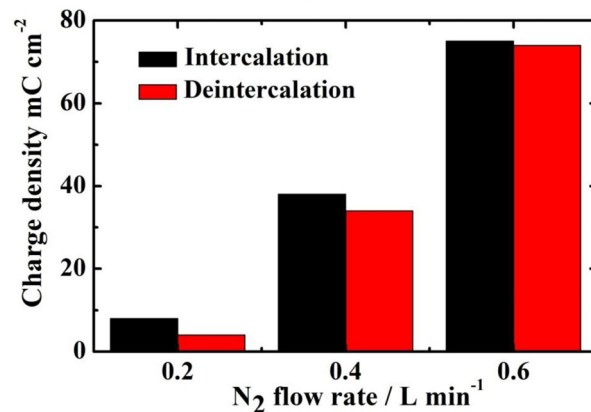
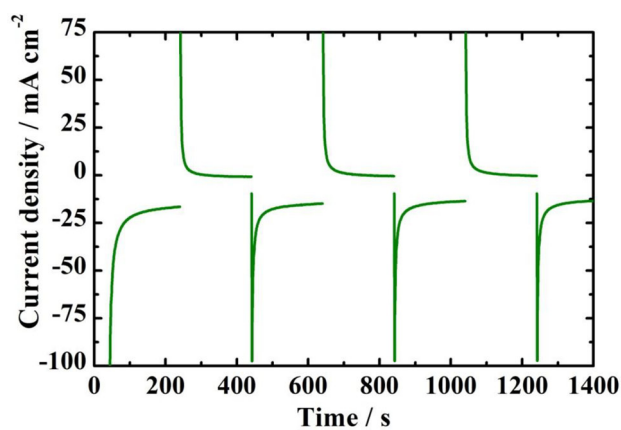


**Figure 7.** The chronoamperometric response recorded at -1 V and -0.2 V for an interval of 200 s of the grown samples at 300 °C for 0.6 L min<sup>-1</sup> N<sub>2</sub> flow rate through the Fe(CO)<sub>5</sub> bubbler (above). Intercalated and deintercalated charge density as a function with the N<sub>2</sub> flow rate through the iron precursor bubbler (below).

lacks the staircase-like shape suggesting less defined transition associated with Li<sup>+</sup>. The capacitance retention after 500 scans

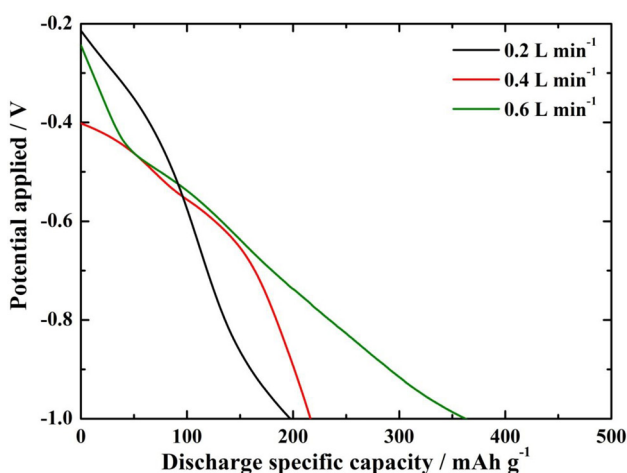


**Figure 8.** The chronopotentiometric curves for the grown samples at 300 °C using 0.2, 0.4 and 0.6 L min<sup>-1</sup> N<sub>2</sub> flow rate through the iron precursor bubbler under constant specific current of 400 mA g<sup>-1</sup> and potential ranging from -0.2 to -1 V.

estimated to be 94% for 0.6 L min<sup>-1</sup>, which is promising for practical applications in Li-ion batteries. The mass of the grown structures was measured by a 5-digit analytical grade scale and obtained by measuring the FTO glass substrate before and after the growth. It was found to be 0.00008, 0.00012 and 0.00028 g for 0.2, 0.4 and 0.6 L min<sup>-1</sup>, respectively.

Others have reported larger specific discharge capacity values than ours (375 mAh g<sup>-1</sup>), but with a significant degradation even after 50 cycles. In particular, Zhang et. al. fabricated fiber-like Fe<sub>2</sub>O<sub>3</sub> macroporous nanomaterials presenting a large discharge capacity of 2750 mAh g<sup>-1</sup> at the first cycle and 732 mAh g<sup>-1</sup> after 50 cycles.<sup>[51]</sup> Also, α-Fe<sub>2</sub>O<sub>3</sub> hollow spheres demonstrated an initial discharge capacity of 1800 mAh g<sup>-1</sup> and 710 mAh g<sup>-1</sup> after 100 cycles.<sup>[52]</sup> On the other hand, microparticles of similar size delivered a much lower capacity of 340 mAh g<sup>-1</sup> at the end of 100 cycles indicating the significant effect of morphology on the cycling performance of the electrodes.<sup>[52]</sup> A one-step template-engaged precipitation method has been invented to synthesize different types of hollow structures including α-Fe<sub>2</sub>O<sub>3</sub> nanotubes.<sup>[53-55]</sup> In particular, the investigation of phase-pure α-Fe<sub>2</sub>O<sub>3</sub> nanotubes for Li-ion batteries demonstrated better performance than α-Fe<sub>2</sub>O<sub>3</sub> nanoparticles showing a value of 1000 mAh g<sup>-1</sup> with capacitance retention after 50 cycles.

Regarding other transition metal oxides, the nanowire Co<sub>3</sub>O<sub>4</sub> arrays maintained a stable capacity of 700 mAh g<sup>-1</sup> after 20 cycles, while commercial Co<sub>3</sub>O<sub>4</sub> powders gave a significantly lower capacity of 80 mAh g<sup>-1</sup> and unsupported nanowires only showed a moderate capacity of 350 mAh g<sup>-1</sup> after 20 cycles.<sup>[56]</sup> Additionally, the discharge capacity of MnO<sub>x</sub>/carbon nanofibers was 785 mAh g<sup>-1</sup> at the first cycle presenting capacitance retention of 76% after 50 cycles.<sup>[57,58]</sup> More recently, the same group also prepared MnO<sub>x</sub>/carbon nanofiber composites through electrodepositing MnO<sub>x</sub> nanoparticles onto electrospun carbon nanofibers. These nanocomposites exhibited a

stable reversible capacity of approximately 500 mAh g<sup>-1</sup> after 50 cycles at 50 mA g<sup>-1</sup>, while at even higher current density of 500 mA g<sup>-1</sup>, a suitable reversible capacity of 400 mAh g<sup>-1</sup> was also obtained.<sup>[59]</sup>

It can be confidently anticipated that the improved storage ability of anodes based on metal oxides is closely related to the surface area, crystallinity and morphology. However, the majority of these materials suffer from large volume change upon Li<sup>+</sup> charging / discharging, which leads to capacity fading even after 50 cycles.

In this work, the chronopotentiometric analysis of α-Fe<sub>2</sub>O<sub>3</sub> electrode has shown unique characteristics, which makes it promising as high performance anode material including the excellent capacitance retention of 94% after 500 scans under constant specific current of 1 A g<sup>-1</sup> indicating both high rate performance and good stability.

To examine the effect of N<sub>2</sub> flow rate on the electron transport and recombination properties of the as-grown α-Fe<sub>2</sub>O<sub>3</sub> coatings, electrochemical impedance spectroscopy (EIS) was performed as indicated in Figure 9. The symbols represent the

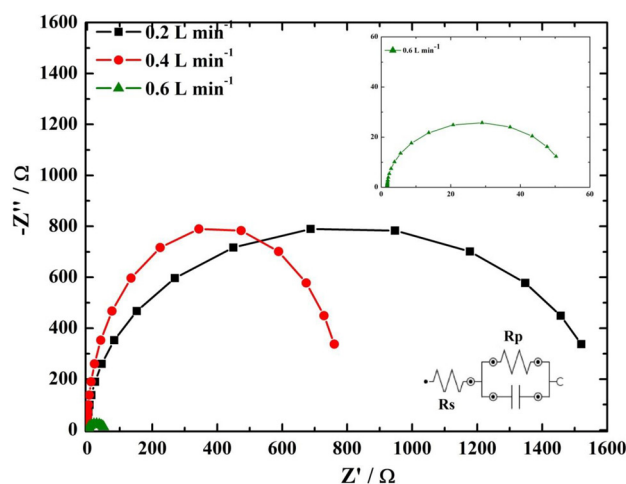


**Figure 9.** Nyquist plots of the measured (plot) and fitted (line) impedance spectra of the samples grown at 300 °C using 0.2, 0.4 and 0.6 L min<sup>-1</sup> N<sub>2</sub> flow rate through the iron precursor bubbler. Equivalent circuit is indicated.

experimental data, while the solid lines, the results fitted by Z-view software. Nyquist plots show semicircles, which correspond to the charge transfer reaction at the anode / electrolyte interface.<sup>[60,61]</sup> The smaller the diameter of the semicircle corresponds to a reduce transfer resistance. The general equivalent circuit used to interpret the data is consisted of a solution resistance ( $R_s$ ), a charge transfer resistance across the interface ( $R_p$ ) and a constant phase element. The fitted values of  $R_p$  are estimated to be 1524 Ω, 760 Ω and 52 Ω for the 0.2 L min<sup>-1</sup>, 0.4 L min<sup>-1</sup> and 0.6 L min<sup>-1</sup>, respectively suggesting that the last one is beneficial for the charge transfer across the α-Fe<sub>2</sub>O<sub>3</sub> / electrolyte interface enhancing its capacitive performance.

### 3. Conclusions

The growth of  $\alpha$ -Fe<sub>2</sub>O<sub>3</sub> with good stability under environmental conditions was carried out by APCVD at 300 °C on FTO glass substrate. An enhancement of the crystallinity along with the presence of porous microstructure composed of compact interconnected nanoparticles about 60 nm was achieved for the highest N<sub>2</sub> flow rate through the iron precursor bubbler. The 0.6 L min<sup>-1</sup> sample presented a charge capability of 75 C cm<sup>-2</sup> with a reversibility of the intercalation / deintercalation processes over a period of 1400 s. Additionally, it presented a specific discharge capacity of 365 mAh g<sup>-1</sup> with capacitance retention of 94% after 500 scans. The improved performance of this sample is due to a combination of the enhanced crystalline quality and the active material exposed to the electrolyte.

On the basis of our results, this APCVD route provides a simple and cost-efficient way to grow  $\alpha$ -Fe<sub>2</sub>O<sub>3</sub> that could be used as promising anodes for Li-ion batteries.

### Supporting information

Experimental Section can be found in the Supporting Information available online.

### Acknowledgements

EPSRC for financial supporting and I.P.P Group.

**Keywords:** Chemical vapor deposition · Fe<sup>III</sup> oxide · Cyclic voltammetry · Electrochemistry

- [1] F. Y. Cheng, Z. L. Tao, J. Liang, J. Chen, *Chem. Mater.* **2008**, *20*, 667–681.
- [2] J. Liu, G. Cao, Z. Yang, D. Wang, D. Dubois, X. Zhou, G. L. Graff, L. R. Pederson, J. –G. Zhang, *Chem. Sus. Chem.* **2008**, *1*, 676–697.
- [3] L. Ji, Z. Lin, M. Alcoutlabi, X. Zhang, *Energy Environ. Sci.* **2011**, *4*, 2682–2699.
- [4] Y. Wang, H. Li, P. He, E. Hosono, H. Zhou, *Nanoscale* **2010**, *2*, 1294–1305.
- [5] L. Ji, M. Rao, H. Zheng, L. Zhang, Y. Li, W. Duan, J. Guo, E. J. Cairns, Y. Zhang, *J. Am. Chem. Soc.* **2011**, *133*, 18522–18525.
- [6] L. Ji, Z. Tan, T. R. Kuykendall, S. Aloni, S. Xun, E. Lin, V. Battaglia, Y. Zhang, *Phys. Chem. Chem. Phys.* **2011**, *13*, 7170–7177.
- [7] B. Zhao, R. Liu, X. Cai, Z. Jiao, M. Wu, X. Ling, B. Lu, Y. Jiang, *J. Appl. Electrochem.* **2014**, *44*, 53–60.
- [8] H. Buqa, D. Goers, M. Holzapfel, M. E. Spahr, P. Novak, *J. Electrochem. Soc.* **2005**, *152*, A474–A481.
- [9] D. Larcher, C. Masquelier, D. Bonnin, Y. Chabre, V. Masson, J. B. Leriche, J. M. Tarascon, *J. Electrochem. Soc.* **2003**, *150*, A133–A139.
- [10] M. F. Hassan, Z. Guo, Z. Chen, H. Liu, *Mater. Res. Bull.* **2011**, *46*, 858–864.
- [11] T. Muraliganth, A. V. Murugan, A. Manthiram, *Chem. Comm.* **2009**, 7360–7362.
- [12] W.–J. Yu, P.–X. Hou, F. Li, C. Liu, *J. Mater. Chem.* **2012**, *22*, 13756–13763.
- [13] Y. Huang, Z. Dong, D. Jia, Z. Guo, W. I. Cho, *Solid State Ionics* **2011**, *201*, 54–59.
- [14] X. J. Zhu, Z. P. Guo, P. Zhang, G. D. Du, R. Zeng, Z. X. Chen, S. Li, H. K. Liu, *J. Mater. Chem.* **2009**, *19*, 8360–8365.
- [15] D. Larcher, D. Bonnin, R. Cortes, I. Rivals, L. Personnaz, J. M. Tarascon, *J. Electrochem. Soc.* **2003**, *150*, A1643–A1650.
- [16] T. Fujii, de F. M. F. , G. A. Sawatzky, F. C. Voogt, T. Hibma, K. Okada, *Phys. Rev. B* **1999**, *59*, 3195–3202.
- [17] P. Li, E. Y. Jiang, H. L. Bai, *J. Phys. D Appl. Phys.* **2011**, *44*, 075003. DOI: <http://dx.doi.org/10.1088/0022-3727/44/7/075003>
- [18] J. Cao, T. Kako, N. Kikugawa, J. Ye, *J. Phys. D Appl. Phys.* **2010**, *43*, 325101. DOI: <http://dx.doi.org/10.1088/0022-3727/43/32/325101>
- [19] K. Woo, H. J. Lee, J. –P. Ahn, Y. S. Park, *Adv. Mater.* **2003**, *15*, 1761–1764.
- [20] T. J. LaTempa, X. Feng, M. Paulose, C. A. Grimes, *J. Phys. Chem. C* **2009**, *113*, 16293–19298.
- [21] A. Duret, M. Grätzel, *J. Phys. Chem. B* **2005**, *109*, 17184–17191.
- [22] Z. Ma, X. Huang, S. Dou, J. Wu, S. Wang, *J. Phys. Chem. C* **2014**, *118*, 17231–17239.
- [23] S. Mathur, M. Veith, V. Sivakov, H. Shen, V. Huch, U. Hartmann, H.–B. Gao, *Chem. Vapor Depos.* **2002**, *8*, 277–283.
- [24] A. Kay, I. Cesar, M. Grätzel, *J. Am. Chem. Soc.* **2006**, *128*, 15714–15721.
- [25] Z. Zhang, B. Q. Wei, P. M. Ajayan, *Appl. Phys. Lett.* **2001**, *79*, 4207–4209.
- [26] M. Sharon, B. M. Prasad, *Sol. Energ. Mater.* **1983**, *8*, 457–469.
- [27] Y. Zhou, Z. Zhang, Y. Yue, *Mater. Lett.* **2005**, *59*, 3375–3377.
- [28] A. A. Tahir, K. G. Upul Wijayantha, S. Saremi-Yarahmadi, M. Mazhar, V. McKee, *Chem. Mater.* **2009**, *21*, 3763–3772.
- [29] H. Gil Cha, C. Woo Kim, Y. Hwan Kim, M. Hyang Jung, E. Sun Ji, B. K. Das, J. Chang Kim, Y. Soo Kang, *Thin Solid Films* **2009**, *517*, 1853–1856.
- [30] K. Shalini, G.N. Subbanna, S. Chandrasekaran, S. A. Shivashankar, *Thin Solid Films* **2003**, *424*, 56–60.
- [31] H. Ago, K. Nakamura, S. Imamura, M. Tsuji, *Chem. Phys. Lett.* **2004**, *391*, 308–313.
- [32] S. Saremi-Yarahmadi, K. G. Upul Wijayantha, A. A. Tahir, B. Vaidhyathan, *J. Phys. Chem. C* **2009**, *113*, 4768–4778.
- [33] C. C. Chai, J. Peng, B. P. Yan, *Sensor. Actuat. B-Chem.* **1996**, *34*, 412–419.
- [34] X. Li, E. Lin, C. Zhang, S. Li, *J. Mater. Chem.* **1995**, *5*, 1953–1956.
- [35] T. D. Manning, I. P. Parkin, R. J. H. Clark, D. Sheel, M. E. Pemble, D. Vernardou, *J. Mater. Chem.* **2002**, *12*, 2936–2939.
- [36] S. Liang, J. Zhu, C. Wang, S. Yu, H. Bi, X. Liu, X. Wang, *Appl. Surf. Surf.* **2014**, *292*, 278–284.
- [37] S. Rai, A. Ikram, S. Sahai, S. Dass, R. Shrivastav, V. R. Satsangi, *Renew. Energ.* **2015**, *83*, 447–454.
- [38] E. Elongovan, K. Ramamurthi, *Thin Solid Films* **2005**, *476*, 231–236.
- [39] M.–C. Huang, W.–S. Chang, J.–C. Lin, Y.–H. Chang, C.–C. Wu, *J. Alloy Comp.* **2015**, *636*, 176–182.
- [40] M. Alagiri, S. B. A. Hamid, *Mater. Lett.* **2014**, *136*, 329–332.
- [41] A. Abdelhakim Ayachi, H. Mechakra, M. MansoSilvan, S. Boudjaadar, S. Achour, *Ceram. Int.* **2015**, *41*, 2228–2233.
- [42] M. Ocăna, J. V. Garcia, *J. Am. Ceram. Soc.* **1992**, *75*, 2010–2012.
- [43] P. Yang, Y. Ding, Z. Lin, Z. Chen, Y. Li, P. Qiang, M. Ebrahimi, W. Mai, C. P. Wong, Z. L. Wang, *Nano Lett.* **2014**, *14*, 731–736.
- [44] T. Yamashita, P. Hayes, *Appl. Surf. Sci.* **2008**, *254*, 2441–2449.
- [45] M. Aronniemi, J. Sainio, J. Lahtinen, *Appl. Surf. Sci.* **2007**, *253*, 9476–9482.
- [46] L. Dghoughi, B. Elidrissi, C. Bernede, M. Addou, M. A. Lamrani, M. Regragui, H. Erguig, *Appl. Surf. Sci.* **2006**, *253*, 1823–1829.
- [47] C. L. Long, L. L. Jiang, T. Wei, J. Yan, Z. J. Fan, *J. Mater. Chem. A* **2014**, *2*, 16678–16686.
- [48] G. S. Gund, D. P. Dubal, N. R. Chodankar, J. Y. Cho, P. Gomez-Romero, C. Park, C. D. Lokhande, *Sci. Rep.* **2015**, *5*, 12454 DOI: 10.1038/srep12454
- [49] D. Louloudakis, D. Vernardou, E. Spanakis, N. Katsarakis, E. Koudoumas, *Surf. Coat. Tech.* **2013**, *230*, 186–189.
- [50] D. Vernardou, M. Apostolopoulou, D. Louloudakis, N. Katsarakis, E. Koudoumas, *J. Colloid Interf. Sci.* **2014**, *424*, 1–6.
- [51] S. L. Liu, L. N. Zhang, J. P. Zhou, J. F. Xiang, J. T. Sun, J. G. Guan, *Chem. Mater.* **2008**, *20*, 3623–3628.
- [52] B. Wang, J. S. Chen, H. B. Wu, Z. Wang, X. W. Lou, *J. Am. Chem. Soc.* **2011**, *133*, 17146–17148.
- [53] Z. Y. Wang, D. Y. Luan, S. Madhavi, C. M. Li, X. W. Lou, *Chem. Commun.* **2011**, *47*, 8061–8063.
- [54] Z. Wang, D. Luan, F. Y. C. Boey, X. W. Lou, *J. Am. Chem. Soc.* **2011**, *133*, 4738–4741.
- [55] Z. Wang, D. Luan, C. M. Li, F. Su, S. Madhavi, F. Y. C. Boey, X. W. Lou, *J. Am. Chem. Soc.* **2010**, *132*, 16271–16277.
- [56] Y. G. Li, B. Tan, Y. Y. Wu, *Nano Lett.* **2008**, *8*, 265–270.
- [57] L. Ji, X. Zhang, *Electrochem. Commun.* **2009**, *11*, 795–798.
- [58] L. Ji, A. J. Medford, X. Zhang, *J. Mater. Chem.* **2009**, *19*, 5593–5601.
- [59] Z. Lin, L. W. Ji, M. D. Woodroof, X. W. Zhang, *J. Power Sources* **2010**, *195*, 5025–5031.
- [60] J. Qin, W. Lv, Z. Li, B. Li, F. Kang, Q. – H. Yang, *Chem. Commun.* **2014**, *50*, 13447–13450.
- [61] Y. Wu, P. Zhu, X. Zhao, M.V. Reddy, S. Peng, B. V. R. Chowdari, S. Ramakrishna, *J. Mater. Chem. A* **2013**, *1*, 852–859.

